

Porous GaP/g-C₃N₄ Photoanode for Enhanced Hydrogen Production

Hao Yuan,^[a] Maojun Zheng,^{*[a]} Ying Yang,^[a] Jiaheng Gao,^[a] Hao Chen,^[a] Yunlong Fan,^[a] Yinghong Li,^[a] Li Ma,^[b] Guohua Wang,^[a] and Wenzhong Shen^[a]

The g-C₃N₄ decorated porous gallium phosphide have been fabricated by a facile electrophoretic deposition (EPD) process. The morphology, element composition and light absorption of the GaP/g-C₃N₄ photoanode were observed using field-emission scanning electron microscopy, X-ray photoelectron spectroscopy, ultraviolet and visible spectrophotometer, respectively. When acting as photoanode, porous GaP/g-C₃N₄ serves as a direct Z-scheme system, where photogenerated holes in GaP are expended by electrons generated from the g-C₃N₄, inhibit-

ing the corrosion of GaP. Therefore, the porous GaP/g-C₃N₄ showed a larger photocurrent density, which is 2.1 times as large as that of the porous GaP without g-C₃N₄, and a more stable photocurrent density for over 10000 s (at 0 V vs RHE). Thus, this work delivers a practical way to improve the photoelectrochemical stability and property of III-V semiconductor materials, which could be used in solar energy conversion fields.

Introduction

Solar photoelectrochemical (PEC) hydrogen production is a reliable approach to handle the energy crisis and environment issues. Since the groundbreaking research on TiO₂ PEC hydrogen production conducted by Fujishima and Honda in 1972,^[1] significant research achievements have been dedicated to find suitable materials for converting solar energy to hydrogen.^[2] III-V compound semiconductors, for instance, GaP,^[3-5] InP,^[6-8] and GaAs,^[9-11] have already gained much concern for their potential applications in energy conversion fields. Among III-V semiconductor materials, GaP (gallium phosphide) is a potential photoelectrochemical semiconductor with an appropriate band gap ($E_g = 2.26$ eV) crossing the oxidation and reduction potentials of water,^[12] enabling the efficient utilization of solar energy.^[13]

Nevertheless, the diffusion length of charge carrier in GaP is short, which causes recombination of photogenerated carrier.^[14] Meanwhile, its indirect bandgap limits the absorption at longer wavelengths.^[15] In order to solve these problems, much attempt has been concentrated on the research of porous GaP. Our team has already produced GaP nanopore arrays by a two-step etching strategy^[16] and a facile one-step electrochemical

etching method^[17] in previous works. Furthermore, we have successfully fabricated transferable three-dimensional GaP nanopore array film.^[18] The porous GaP can decrease the minority carrier recombination by reducing the distance from the position where photoinduced carrier has been generated to the photoelectrode surface, and improve the light absorption by allowing incident light scatter within the nanopore. However, the porous GaP faces stability problems during PEC hydrogen production. In order to improve the stability of porous GaP and further enhance its photocatalytic activity, depositing an appropriate material on the surface of porous GaP is an efficient method.

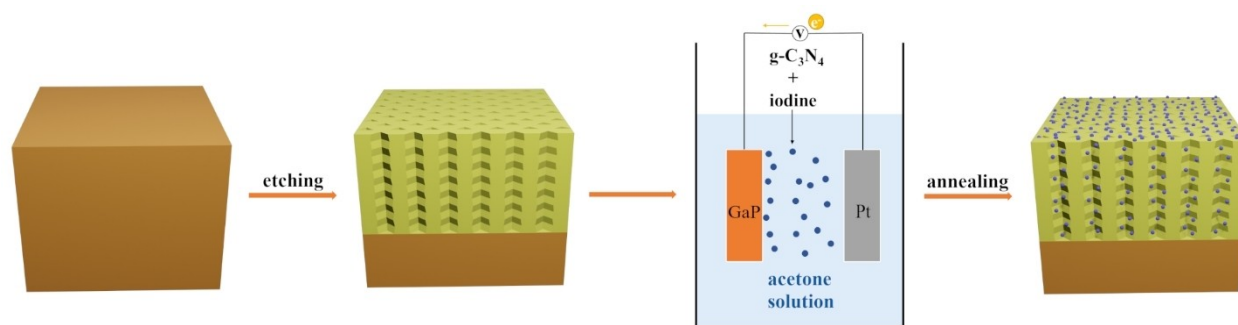
Graphitic carbon nitride (g-C₃N₄), a typical two-dimension structure n-type metal-free semiconductors, has drawn extensive attention in PEC or photocatalytic (PC) field.^[19-21] The g-C₃N₄ with a narrow bandgap (2.7 eV) has many advantages such as facile production, nontoxicity, high chemical stability and natural abundance.^[22-24] By combining g-C₃N₄ and other semiconductors, heterojunctions with great PEC performance can be constructed. Recently, Mohamed et al.^[25] constructed g-C₃N₄/ThO₂@BiVO₄ photoanode with a 'spongy' and 'needle-like' nano-floer architecture, which exhibited exceptional performance and photostability. Liang et al.^[26] fabricated Ni-ZnO@C/g-C₃N₄ core-double shell microspheres with prominent photocatalytic hydrogen evolution performance using self-sacrificing template method.

The construction of heterojunctions can be achieved through various methods, including hydrothermal, atomic layer deposition and electrodeposition. Among these techniques, electrophoretic deposition (EPD) is recognized as an effective method for depositing composites.^[27-29] Different from electrolytic deposition (ELD), the EPD is based on solutions of macromolecules or colloidal suspensions rather than ionic species. The charged particles in the suspension transport to the electrode with an opposite charge under an applied electric field, resulting in the formation of a film on the surface of the

[a] Dr. H. Yuan, Prof. M. Zheng, Dr. Y. Yang, J. Gao, H. Chen, Y. Fan, Y. Li, G. Wang, Prof. W. Shen
Key Laboratory of Artificial Structures and Quantum Control (Ministry of Education), School of Physics and Astronomy
Shanghai Jiao Tong University
Shanghai 200240, P.R. China
E-mail: mjzheng@sjtu.edu.cn

[b] Prof. L. Ma
School of Chemistry and Chemical Technology
Shanghai Jiao Tong University
Shanghai 200240, P.R. China

Supporting information for this article is available on the WWW under <https://doi.org/10.1002/cnma.202400024>



Scheme 1. A schematic illustration for the synthetic process of the porous GaP/g-C₃N₄.

electrode.^[30] The application of electrophoretic deposition in the synthesis of composite materials for water splitting has been extensively investigated in many studies.^[31,32]

In this study, we report a facile electrophoretic deposition (EPD) method to deposit g-C₃N₄ on porous GaP. As is illustrated in Scheme 1, porous GaP were fabricated on the GaP wafer substrate via electrochemical etching. Later, the g-C₃N₄ were deposited on the porous GaP substrate by an EPD process, followed by annealing under argon atmosphere. This strategy can greatly enhance the stability of porous GaP. Porous GaP with g-C₃N₄ can exhibited stable PEC water splitting behaviour after 10000 s. Moreover, the porous GaP with g-C₃N₄ possesses higher catalytic efficiency. This work may have potential applications in improving the stability and performance of III–V semiconductor materials, contributing to advancements in the field of solar energy conversion.

Results and Discussion

To investigate the crystalline structure and phase of the GaP/g-C₃N₄, XRD patterns are shown in Figure 1. Two diffraction peaks can be seen at $2\theta = 13.1^\circ$ and $2\theta = 27.5^\circ$ in g-C₃N₄, which accord with the (100) and (002) diffraction planes of g-C₃N₄ (JCPDS

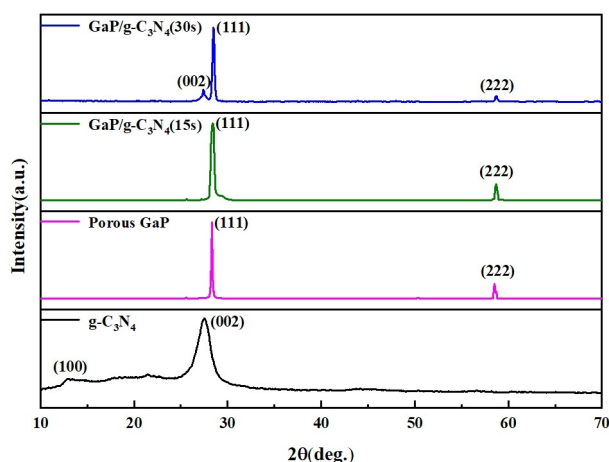


Figure 1. XRD patterns of g-C₃N₄, porous GaP and GaP/g-C₃N₄.

card No.87-1526). The XRD patterns of the porous GaP corresponded to the zinc blende GaP (JCPDS Card 32-0397). Finally, with increasing the EPD time, GaP/g-C₃N₄ sample shows a mixed crystallinity composed of porous GaP and g-C₃N₄. The diffraction peak of g-C₃N₄ located at $2\theta = 27.5^\circ$ can be found in GaP/g-C₃N₄, indicating the successful formation of composites by EPD and annealing process.

The high magnification top-view SEM image of the porous GaP/g-C₃N₄ in Figure 2(a) shows the presence of triangular-shaped pores, with the side length ranging from approximately 200 nm to 500 nm. The image shows no significant g-C₃N₄ aggregation on top of the of GaP pores, indicating that this method effectively suppresses the accumulation of nanoparticles at pore entrances, preventing pore blocking. As shown in Figure 2(b), the cross-sectional view image demonstrates that the inner wall of the pore exhibits a three-dimensional structure. The structural features of porous GaP/g-C₃N₄ can enhance light absorption, increase the surface area and facilitate the separation of photogenerated carriers due to the distinctive geometric construction, leading to an improvement in the PEC property. Element distributions of the cross-sectional were analyzed via mapping analysis, as can be seen in Figure 2(c–f), which shows the EPD g-C₃N₄ distribute evenly in the side walls of the porous GaP.

To analyse the chemical state of the porous GaP/g-C₃N₄, we conducted the X-ray photoelectron spectroscopy (XPS) measurements. The survey spectra (Figure 3(a)) of the porous GaP/g-C₃N₄ indicate the existence of Ga, P, C, N and O. The peaks at 20 eV and 20.8 eV in Ga 3d spectrum (Figure 3(b)) correspond to the Ga 3d_{5/2} and Ga 3d_{3/2}, respectively. While the signals at 130.4 eV and 129.5 eV in Figure 3(c) could arise from P 2p_{1/2} and P 2p_{3/2}. Above findings are consistent with the characteristic peaks of GaP.^[33] Additionally, the presence of the native oxide signal at 22.1 eV (Figure 3(b)) suggests partial oxidation of the active GaP surface. Moreover, a peak at 25.4 eV can be ascribed to the hybridization between surface states of Ga 3d and O 2s.^[34] The other peak located at 133.35 eV (Figure 3(c)) could be assigned to native oxide P–O.^[35] The observed oxidation peaks are derived from easy oxidation of GaP even at room temperature. To further confirm the oxidation states of porous GaP/g-C₃N₄, O 1s spectrum is shown in Figure 3(f). The signal at 532.1 eV is attributed to Ga–O–Ga and O_n–Ga–(OH)_{3–n}. The peak

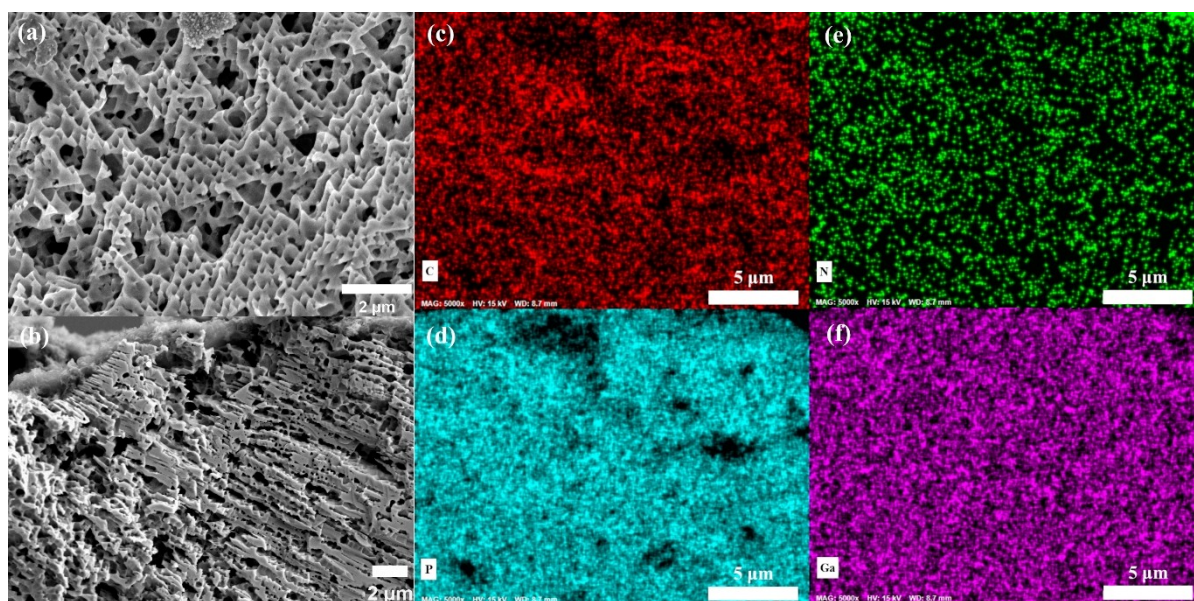


Figure 2. (a) Top view SEM image of the porous GaP/g-C₃N₄. (b) Cross-sectional SEM image of the porous GaP/g-C₃N₄. (c-f) EDX elemental mapping of C, N, P and Ga.

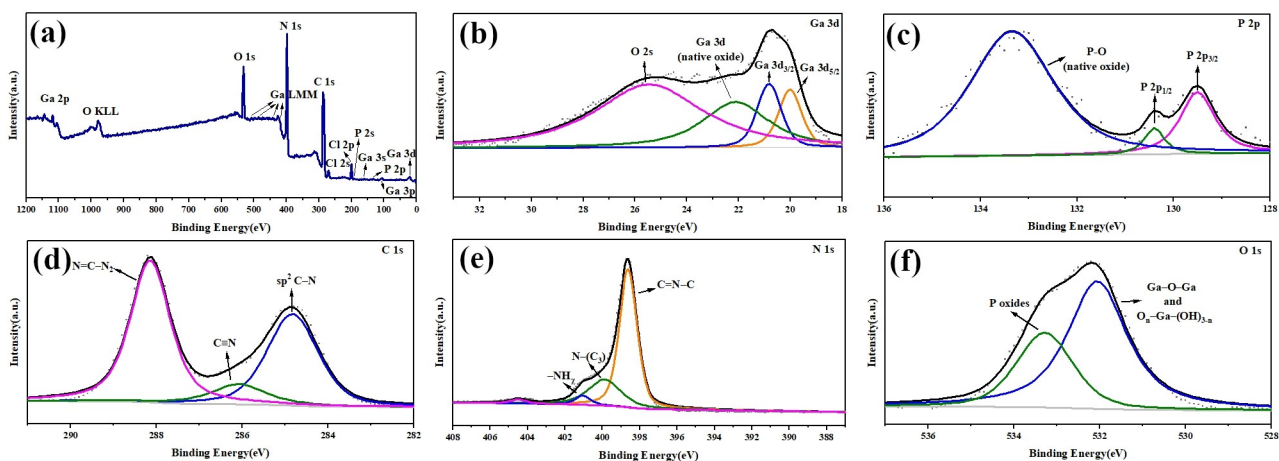


Figure 3. (a) XPS survey spectrum, and high-resolution XPS spectra of (b) Ga 3d, (c) P 2p, (d) C 1s, (e) N 1s, and (f) O 1s for porous GaP/g-C₃N₄.

located at 533.28 eV corresponds to P oxides.^[36] The C1s spectrum shown in Figure 3(d) exhibits three peaks at 284.8, 286.1 and 288.2 eV. The main binding energy peak is observed at 288.2 eV, which can be assigned to N=C-N₂ bonds in striazine ring (C₃N₃) units or heptazine (C₆N₇) units. Additionally, a peak corresponding to C≡N appears at 286.1 eV.^[37] Furthermore, the C1s peak at 284.8 eV is commonly associated with graphitic carbon or sp² C-N.^[38] The N 1s spectrum in Figure 3(e) composed of binding energies, which can be deconvoluted into four distinct peaks: the sp² N of striazine ring units or heptazine units (C=N-C, 398.6 eV), tertiary nitrogen (N-(C₃), 399.9 eV), amino functions (-NH₂, 401.1 eV), and the peak at 404.5 eV may be attributed to charging effects.^[39]

Photoluminescence spectroscopy was performed on all porous GaP with varied g-C₃N₄ EPD time. As GaP is indirect bandgap semiconductor, the GaP has a low PL intensity. The

signal observed in porous GaP was found to be higher than that of planar GaP (Figure 4(a) inset), indicating an enhanced recombination of photoinduced carrier attributed to the presence of surface state defects. As shown in Figure 4(a), the PL intensity of porous GaP/g-C₃N₄ significantly increased compared to the GaP without g-C₃N₄. The peak positions were about 440 nm, which align with the PL spectra of g-C₃N₄.^[40] Therefore, the much stronger PL signal of porous GaP/g-C₃N₄ can be ascribed to the signal of g-C₃N₄.

The total reflectance spectra of the planar GaP, porous GaP and GaP/g-C₃N₄ is shown in Figure 4(b), the wavelength range is 250–850 nm. All the GaP samples showed a lower reflection in the wavelength shorter than 500 nm after etching, as a result of light trapping effect of nanopore structure. The photons within this wavelength range have the capability to excite the valence band electrons in GaP, achieving enhanced photo-

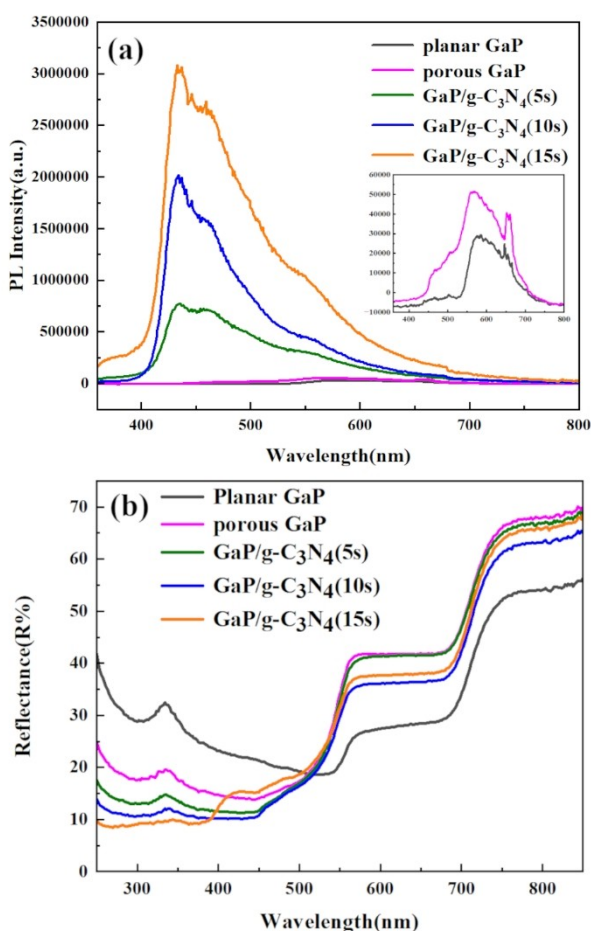


Figure 4. (a) Room temperature photoluminescence spectra of porous GaP and GaP/g-C₃N₄ with different EPD times. (b) Reflectance spectra of porous GaP and GaP/g-C₃N₄ with different EPD times.

chemical performance. The light reflection of GaP/g-C₃N₄ (5 s and 10s) was further reduced compared to the porous GaP. The enhanced antireflection property of the porous GaP/g-C₃N₄ is due to the g-C₃N₄ on nanopore wall that facilitate strong light absorption, scattering and trapping. However, with the increasing of EPD time of g-C₃N₄, reflection intensity of porous GaP/g-C₃N₄ (15 s) was increased in the wavelength range 400–500 nm. This phenomenon can be ascribed to the excessive loaded g-C₃N₄ hindering the light absorption of porous GaP.

Figure 5(a) shows the current density-potential (*J*-*V*) curve of porous GaP and porous GaP/g-C₃N₄ photoanode under simulated solar light illumination. It can be seen that the porous GaP/g-C₃N₄ photoanode shows superior performance over porous GaP photoanode. Under illumination, the current density of porous GaP/g-C₃N₄(10s) photoanode is 0.63 mA/cm² at 0 V vs RHE, while that of porous GaP photoanode was 0.29 mA/cm² at 0 V vs RHE. The photocurrent density of porous GaP/g-C₃N₄ initially enhanced with the increasing electrophoretic deposition (EPD) time and arrived the maximum value at 10s, then reduced when EPD continued. The decreased photocurrent density of porous GaP/g-C₃N₄ (15 s) photoanode is ascribed to the excessive loaded g-C₃N₄ hindering the light

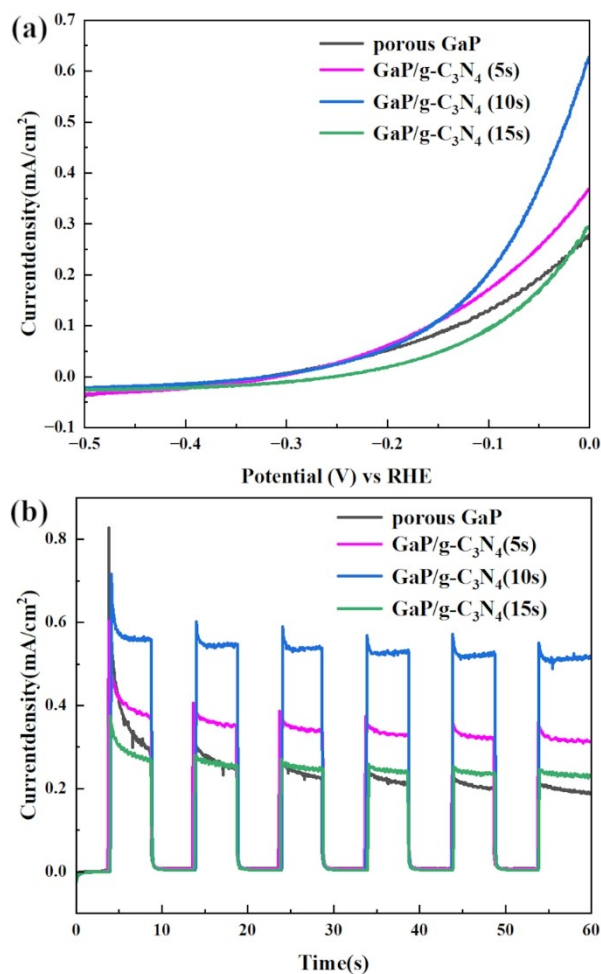


Figure 5. PEC performance of the GaP/g-C₃N₄ in 0.35 M Na₂S and 0.25 M Na₂SO₃ solution (pH = 13.35) under illumination of 100 mW/cm². (a) Linear sweep voltammetry of GaP/g-C₃N₄ with different EPD times. (b) Amperometric *I*-*t* curves (at 0 V vs. RHE) of the GaP/g-C₃N₄ with different EPD times.

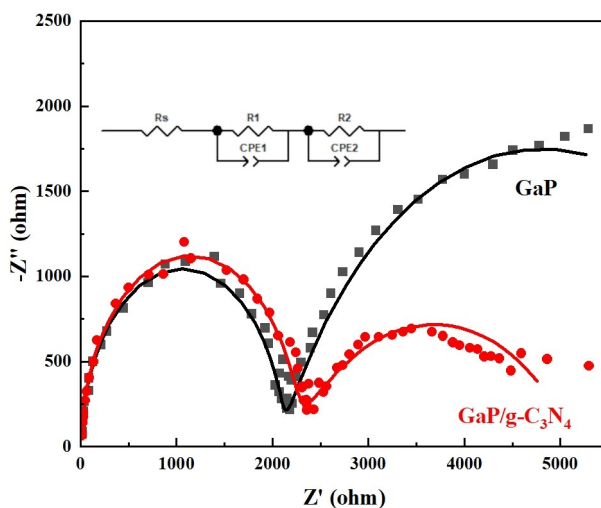


Figure 6. Nyquist plots of porous GaP and GaP/g-C₃N₄ photoanode. The experimental data is represented by scatter points in the plots, while the fitted curves using the equivalent circuit model inset are depicted by solid lines.

adsorption of porous GaP, which is in accord with the reflectance spectra.

To study the photoresponse of porous GaP/g-C₃N₄, the transient photocurrent of GaP/g-C₃N₄ photoanode was tested at 0 V versus RHE under repeated on-off illumination cycle (Figure 5(b)). As a result of the transient effect in light excitation, a large initial peak current was observed in all photoanode upon illumination, then reached the steady state quickly. After the light is switched off, the photocurrent rapidly decays to zero. These phenomena indicate the GaP/g-C₃N₄ photoanode has rapid light response and wonderful switching performance. The steady state photocurrent density of porous GaP with g-C₃N₄ EPD time of 10s is 0.52 mA/cm², which is larger than that of porous GaP/g-C₃N₄ (0 s, 5 s and 15 s). This further authorized the good performance for the g-C₃N₄ EPD. Besides, typical current spikes were noticed during the repeated illumination cycles. These spikes indicate some photogenerated holes accumulate at photoanode surface and were not injected into electrolyte,^[41] which may be due to slow oxidation reaction at the interface,^[42] or carrier oxidized trap states in photoanode.^[43] The spikes are significant suppressed after g-C₃N₄ deposition, which is attribute to the improved interface charge transport kinetics.

Electrochemical impedance spectroscopy (EIS) was performed on porous GaP and GaP/g-C₃N₄ to further understand the enhancement principle of PEC performance. The scatter points in Figure 6 are measured data, and solid curves are fitted curve which fitted well with porous GaP and GaP/g-C₃N₄. As shown in Figure 6, the GaP/g-C₃N₄ has a smaller impedance arc radius than porous GaP, suggesting a smaller charge resistance and enhanced carrier separation efficiency.

Equivalent circuit model can be seen in Figure 6 inset. In this model, R_s is the bulk resistive loss of electrode. R₁ and CPE₁ represents the internal charge transfer resistance and the depletion layer capacitance, which fitted with high frequency range semicircle. While R₂ and CPE₂ correspond to the low frequency range semicircle, attributing to the charge transfer resistance and double layer capacitance in the electrolyte side.

The summarization of fitted data for each component is shown in Table 1. Two constant phase elements (CPE) can be represented as a non-ideal capacitor. After g-C₃N₄ EPD to the porous GaP, the value of R₂ is reduced and CPE₂ is increased, which means that the variation of charge transfer resistance and capacitance mostly occur at the GaP/g-C₃N₄/electrolyte interface. Therefore, we can assume that EPD g-C₃N₄ facilitates the charge separation and OER on the surface of GaP photoanode.

To investigate stability of porous GaP/g-C₃N₄, photocurrent density at 0 V (vs RHE) under continuous simulated solar light illumination was measured (Figure 7). The photocurrent for the

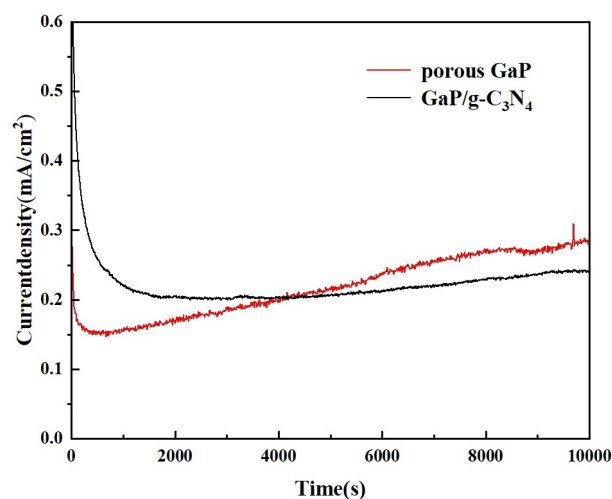


Figure 7. Current density under constant light illumination versus time (stability performance) of porous GaP and GaP/g-C₃N₄ photoanode (at 0 V vs. RHE).

porous GaP electrode increased to nearly 183% compare to the initial steady state current after 10000 s. The increasing photocurrent can be ascribed to corrosion current of porous GaP in electrolyte under illumination. The migration of photoinduced holes to electrolyte were insufficiently, resulting in the oxidation of electrolyte and GaP reacted simultaneously. In contrast, the porous GaP/g-C₃N₄ remained stable compare to the initial steady state photocurrent after 10000 s. Figure S1 shows the SEM images of porous GaP and GaP/g-C₃N₄ after prolonged stability. After the test, the porous GaP exhibited serious corrosion and experienced severe structural damage. Due to the higher oxidation potential of GaP than that of water, photogenerated holes tend to induce GaP self-oxidation, resulting in corrosion of GaP. In contrast, GaP/g-C₃N₄ exhibited minimal structural damage after stability test. The improved photostability can be attributed to GaP/g-C₃N₄ heterojunction, where photogenerated holes in GaP were consumed by photo-generated electrons from g-C₃N₄, suppressing the corrosion of GaP. Consequently, the stability of GaP/g-C₃N₄ have been greatly improved.

A schematic diagram (Figure 8) is presented to explain the mechanism of PEC hydrogen production from water with porous GaP/g-C₃N₄ photoelectrode.^[23] The porous GaP/g-C₃N₄ photoanodes act as a direct Z-scheme system. Upon illumination, electron-hole pairs are produced both in g-C₃N₄ and GaP. Photoinduced hole in valence band of GaP was expended by electron generated from conduction band of g-C₃N₄, which not only facilitates the separation of photogenerated electron-hole pairs, but also provides protection against corrosion for porous

Table 1. Resistances and capacitances derived from Nyquist plots.

Sample	R _s (Ω)	R ₁ (Ω)	CPE ₁ (nF)	R ₂ (Ω)	CPE ₂ (μF)
porous GaP	5.33 ± 0.20	2080 ± 24.66	25.23 ± 1.92	5449 ± 447.87	53.07 ± 4.93
GaP/ g-C ₃ N ₄	2.57 ± 0.26	2194 ± 47.52	24.45 ± 2.55	2975 ± 216.72	96.26 ± 12.42

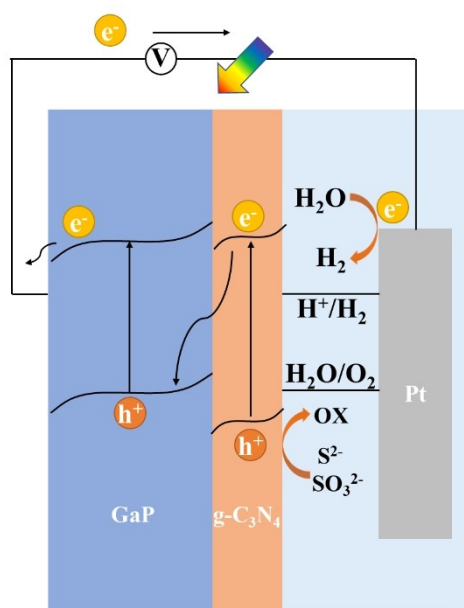


Figure 8. Schematic diagram of PEC process of porous GaP/g-C₃N₄ under light illumination.

GaP. Simultaneously, the holes generated from g-C₃N₄ were consumed by the sacrificial agents (S²⁻ and SO₃²⁻), while the photogenerated electrons in GaP migrate to Pt electrode and react with water. The reaction equations of hydrogen generation are discussed in the supporting information.

Conclusions

In summary, porous GaP decorated with g-C₃N₄ was produced by a facile electrophoretic deposition (EPD) method. The as-prepared GaP/g-C₃N₄ photoanode showed excellent performance for PEC hydrogen production, the photoelectrochemical stability has greatly improved and the maximum photocurrent is 2.1 times compared to the porous GaP without g-C₃N₄ (at 0 V vs RHE). Such large improvement can be ascribed to the porous GaP/g-C₃N₄ heterojunction acting as a direct Z-scheme system. The photoinduced holes in valence band of GaP were expended by electrons generated from conduction band of g-C₃N₄, suppressing the corrosion of porous GaP. We suggest that the g-C₃N₄ decorated porous GaP and the facile electrophoretic deposition (EPD) process may delivers a practical way to improve the stability and performance of III-V semiconductor materials, and find other application in solar energy conversion fields.

Experimental Section

Materials

All chemicals employed in the investigation were analytically pure and utilized as original without any additional purification steps.

The wafers used are sulfur doped single crystal n-GaP purchased from GRINM, with (111) orientation and a carrier concentration of (2–7) × 10¹⁷ cm⁻³. The thickness of the wafer is 300 μm. The wafer was cut into 5 mm×5 mm sample sizes, and subsequently subjected to ultrasonic cleaning in acetone and ethanol to eliminate surface oil contamination, followed by rinsing with deionized water. Subsequently, an Au film was deposited on the backside of the GaP through electron beam evaporation for achieving ohmic contact. Next, high purity silver paint was employed to establish an electrical contact between the Au film and copper wire. After which, epoxy was applied to completely cover the backside of the GaP and the copper wire, ensuring that only the front surface of GaP electrode react with the electrolyte while preventing any leakage current.

Preparation of Porous GaP

Porous GaP were produced on GaP wafer by electrochemical etching according to our previous report.^[17] A two-electrode configuration was used for electrochemical etching, where graphite electrode served as the cathodic electrode and GaP wafer acted as anodic electrode respectively. The prepared GaP electrodes are immersed in 1 M NaBr solution at 4 °C for electrochemical etching. The etching process was carried out at a scan rate of 20 mV/s with a voltage range from 0 to 25 V. The entire etching process was conducted in darkness with continuously stirring. After etching, the color of GaP electrode changes from orange to yellow.

Preparation of g-C₃N₄ NPs

The g-C₃N₄ nanoparticles were obtained using liquid exfoliated techniques. At first, annealing melamine at 550 °C (air) for 4 h with a heating rate of 10 °C/min. The obtained g-C₃N₄ sample was then ground into powder and dispersed in isopropanol under ultrasonication process for about 10 hours. The resultant solution was separated by centrifuge process and dried at 60 °C to evaporated unwanted solvent.

Preparation of Porous GaP/g-C₃N₄

As shown in Scheme 1, the g-C₃N₄ nanoparticles were deposited on the porous GaP substrate via an electrophoretic deposition (EPD) process. 15 mg of g-C₃N₄ was dispersed in 50 mL of acetone under ultrasonication process for 5 min. Next, 10 mg of iodine added to the suspension and sonicated for 15 min, this suspension then used for EPD. The added iodine reacted with acetone then gave H⁺, thus led particles positively charged.^[44] In EPD procedure, the Pt electrode and porous GaP served as anode and cathode. The working and counter electrode were placed parallel in the suspension. Next, porous GaP was deposited by g-C₃N₄ at the deposition potential of 50 V for different length of time. The obtained samples were subjected to a 60 min annealing process at 120 °C in argon environment.

Materials Characterization

The X-ray diffraction analysis of the samples was performed by an X-ray diffractometer (XRD; HaoYuan DX-2700BH multifunction X-ray diffractometer, China) with Cu K_α radiation (λ = 1.54 Å). The morphology of porous GaP/g-C₃N₄ was observed using a cryogenic electron microscopy (GeminiSEM 300, at room temperature), while Energy-dispersive X-ray (EDX) spectroscopy was used to confirm their chemical compositions. The chemical states of the sample were analysed using X-ray photoelectron spectroscopy (XPS,

*ESXCALAB Xi+, Thermo Scientific, America). Room-temperature photoluminescence (PL) spectra of the samples were analysed by the FLS1000 Steady State and Transient State Fluorescence Spectrometer with an excitation wavelength of 365 nm. Additionally, the reflectance spectrum was obtained using an ultraviolet and visible spectrophotometer (PerkinElmer Lambda 950), which includes a photomultiplier, an iodine-tungsten and deuterium lamp, and a 150 mm integrating sphere.

Photoelectrochemical Measurements

The performance of PEC was measured using an electrochemical workstation (PARSTAT 4000) in a standard three-electrode electrochemical set-up (Ag/AgCl, porous GaP/g-C₃N₄ and Pt mesh used as reference electrode, working electrode and counter electrode) containing 0.35 M Na₂S and 0.25 M Na₂SO₃ solution (pH = 13.35). The PEC experiment was obtained under simulated solar light illumination (100 mW/cm², AM 1.5G) provided by SOLAR DGE 700 simulator, and all three electrodes were placed in a quartz cell. The scan rate of the J–V measurement was 20 mV/s, which swept linearly from –1.5 to –1 V vs Ag/AgCl. Chronoamperometry measurement was performed under the same illumination at –1 V vs Ag/AgCl. All potentials mentioned are reported relative to Ag/AgCl and can be converted to RHE using the Nernstian relation $E_{\text{RHE}} = E_{\text{Ag/AgCl}} + 0.059 \times \text{pH} + E_{\text{Ag/AgCl}}^{\circ}$, where $E_{\text{Ag/AgCl}}^{\circ}$ is 0.1976 V which represents the standard potential of Ag/AgCl at room temperature (25 °C), $E_{\text{Ag/AgCl}}$ is the measured potential versus Ag/AgCl reference electrode, and E_{RHE} represents the convert potential against the RHE. Electrochemical impedance spectroscopy (EIS) data were all measured under simulated solar light illumination at open circuit potential (OCP) within the frequency range from 10⁵ to 10^{–1} Hz, and AC perturbation amplitude is 10 mV.

Supporting Information

The authors have cited additional references within the Supporting Information.^[45,46]

Acknowledgements

This research received funding from the Science and Technology Commission of Shanghai Municipality (Grant no. 21ZR1434900) and National Natural Science Foundation of China (Grant no. 11574203). Besides, we would like to extend our appreciation to the Instrumental Analysis Center of Shanghai Jiao Tong University (IAC-SJTU) for the tests.

Conflict of Interests

The authors have no conflicts of interest to declare.

Data Availability Statement

The data that support the findings of this study are available from the corresponding author upon reasonable request.

Keywords: photoelectrochemical · porous GaP/g-C₃N₄ · direct Z-scheme · hydrogen · water splitting

- [1] A. Fujishima, K. Honda, *Nature* **1972**, 238, 37–38.
- [2] S. Tiwari, N. Jhamb, S. Kumar, A. K. Ganguli, *ChemNanoMat*. **2022**, 8.
- [3] C. Liu, J. Sun, J. Tang, P. Yang, *Nano Lett.* **2012**, 12, 5407–5411.
- [4] M. Malizia, B. Seger, I. Chorkendorff, P. C. K. Vesborg, *J. Mater. Chem. A*. **2014**, 2, 6847–6853.
- [5] A. Standing, S. Assali, L. Gao, M. A. Verheijen, D. van Dam, Y. Cui, P. H. Notten, J. E. Haverkort, E. P. Bakkers, *Nat. Commun.* **2015**, 6, 7824.
- [6] L. Chen, J. Yang, S. Klaus, L. J. Lee, R. Woods-Robinson, J. Ma, Y. Lum, J. K. Cooper, F. M. Toma, L. W. Wang, I. D. Sharp, A. T. Bell, J. W. Ager, *J. Am. Chem. Soc.* **2015**, 137, 9595–9603.
- [7] K. Sun, Y. Kuang, E. Verlage, B. S. Brunschwig, C. W. Tu, N. S. Lewis, *Adv. Energy Mater.* **2015**, 5.
- [8] Q. Li, M. Zheng, L. Ma, M. Zhong, C. Zhu, B. Zhang, F. Wang, J. Song, L. Ma, W. Shen, *ACS Appl. Mater. Interfaces* **2016**, 8, 22493–22500.
- [9] P. Varadhan, H. C. Fu, Y. C. Kao, R. H. Horng, J. H. He, *Nat. Commun.* **2019**, 10, 5282.
- [10] S. Cao, Z. Kang, Y. Yu, J. Du, L. German, J. Li, X. Yan, X. Wang, Y. Zhang, *Adv. Energy Mater.* **2020**, 10.
- [11] W. Yu, M. H. Richter, E. Simonoff, B. S. Brunschwig, N. S. Lewis, *J. Mater. Chem. A* **2021**, 9, 22958–22972.
- [12] M. Gratzel, *Nature* **2001**, 414, 338–344.
- [13] S. Hu, M. R. Shaner, J. A. Beardlee, M. Lichterman, B. S. Brunschwig, N. S. Lewis, *Science*. **2014**, 344, 1005–1009.
- [14] M. J. Price, S. Maldonado, *J. Phys. Chem. C* **2009**, 113, 11988–11994.
- [15] M. G. Walter, E. L. Warren, J. R. McKone, S. W. Boettcher, Q. Mi, E. A. Santori, N. S. Lewis, *Chem. Rev.* **2010**, 110, 6446–6473.
- [16] C. Zhu, M. Zheng, Z. Xiong, H. Li, W. Shen, *Int. J. Hydrogen Energy* **2014**, 39, 10861–10869.
- [17] P. Liu, M. Zheng, Q. Li, L. Ma, F. Wang, D. Jiang, J. Song, Y. You, L. Ma, W. Shen, *Chem. Commun. (Camb.)* **2017**, 53, 12333–12336.
- [18] H. Yuan, M. Zheng, P. Liu, Q. Li, F. Li, D. Jiang, Y. You, W. Zhang, L. Ma, W. Shen, *Microporous Mesoporous Mater.* **2021**, 312.
- [19] S. Panimalar, R. Uthrakumar, E. T. Selvi, P. Gomathy, C. Inmozhi, K. Kaviyarasu, J. Kennedy, *Surf. Interfaces* **2020**, 20.
- [20] L. Xu, S. Ling, H. Li, P. Yan, J. Xia, J. Qiu, K. Wang, H. Li, S. Yuan, *Sens. Actuators B* **2017**, 240, 308–314.
- [21] P. Wen, Y. Sun, H. Li, Z. Liang, H. Wu, J. Zhang, H. Zeng, S. M. Geyer, L. Jiang, *Appl. Catal. B* **2020**, 263.
- [22] W. J. Ong, L. L. Tan, Y. H. Ng, S. T. Yong, S. P. Chai, *Chem. Rev.* **2016**, 116, 7159–7329.
- [23] M. Karimi-Nazarabad, E. K. Goharshadi, S. J. Mahdizadeh, *J. Phys. Chem. C* **2019**, 123, 26106–26115.
- [24] S. Gopalakrishnan, G. M. Bhalerao, K. Jeganathan, *ACS Sustainable Chem. Eng.* **2019**, 7, 13911–13919.
- [25] N. A. Mohamed, A. F. Ismail, T. S. Kiong, M. A. Mat Teridi, *Int. J. Hydrogen Energy* **2024**, 59, 1063–1079.
- [26] S. Liang, G. Sui, D. Guo, Z. Luo, R. Xu, H. Yao, J. Li, C. Wang, *J. Colloid Interface Sci.* **2023**, 635, 83–93.
- [27] R. Sikkema, K. Baker, I. Zhitomirsky, *Adv. Colloid Interface Sci.* **2020**, 284, 102272.
- [28] S. Hu, W. Li, H. Finklea, X. Liu, *Adv. Colloid Interface Sci.* **2020**, 276, 102102.
- [29] M. Atiq Ur Rehman, Q. Chen, A. Braem, M. S. P. Shaffer, A. R. Boccaccini, *Int. Mater. Rev.* **2020**, 66, 533–562.
- [30] F. Bouyer, A. Foissy, *J. Am. Ceram. Soc.* **2004**, 82, 2001–2010.
- [31] P. Zhang, X. F. Lu, D. Luan, X. W. D. Lou, *Angew. Chem. Int. Ed. Engl.* **2020**, 59, 8128–8132.
- [32] B. Chakraborty, R. Beltrán-Suito, J. N. Hausmann, S. Garai, M. Driess, P. W. Menezes, *Adv. Energy Mater.* **2020**, 10.
- [33] V. P. H. Huy, S. So, I. T. Kim, J. Hur, *Energy Storage Mater.* **2021**, 34, 669–681.
- [34] C. Huang, W. Mu, H. Zhou, Y. Zhu, X. Xu, Z. Jia, L. Zheng, X. Tao, *RSC Adv.* **2018**, 8, 6544–6550.
- [35] G. Hollinger, E. Bergignat, J. Joseph, Y. Robach, *J. Vac. Sci. Technol. A: Vacuum, Surfaces, and Films* **1985**, 3, 2082–2088.
- [36] X. Zhang, S. Ptasinska, *Top. Catal.* **2015**, 59, 564–573.
- [37] V. N. Khabashesku, J. L. Zimmerman, J. L. Margrave, *Chem. Mater.* **2000**, 12, 3264–3270.
- [38] Y. Cui, J. Zhang, G. Zhang, J. Huang, P. Liu, M. Antonietti, X. Wang, *J. Mater. Chem.* **2011**, 21.

- [39] A. Thomas, A. Fischer, F. Goettmann, M. Antonietti, J.-O. Müller, R. Schlögl, J. M. Carlsson, *J. Mater. Chem.* **2008**, *18*.
- [40] K. Kočí, H. Dang Van, M. Edelmánová, M. Reli, J. C. S. Wu, *Appl. Surf. Sci.* **2020**, *503*.
- [41] H. Dotan, K. Sivula, M. Grätzel, A. Rothschild, S. C. Warren, *Energy Environ. Sci.* **2011**, *4*, 958–964.
- [42] M. P. Dare-Edwards, J. B. Goodenough, A. Hamnett, P. R. Trellick, *J. Chem. Soc. Faraday Trans. 1* **1983**, *79*.
- [43] G. Horowitz, *J. Electroanal. Chem. Interfacial Electrochem.* **1983**, *159*, 421–436.
- [44] E. S. Kim, N. Nishimura, G. Magesh, J. Y. Kim, J. W. Jang, H. Jun, J. Kubota, K. Domen, J. S. Lee, *J. Am. Chem. Soc.* **2013**, *135*, 5375–5383.
- [45] H. Park, W. Choi, M. R. Hoffmann, *J. Mater. Chem.* **2008**, *18*.
- [46] S. Banerjee, S. K. Mohapatra, P. P. Das, M. Misra, *Chem. Mater.* **2008**, *20*, 6784–6791.

Manuscript received: January 12, 2024
 Revised manuscript received: April 26, 2024
 Accepted manuscript online: May 31, 2024
 Version of record online: July 11, 2024